Full Length Article

Modeling of exhaust gas cleaning by acid pollutant conversion to aerosol particles

Tinja Olenius [a,b,*], Arto Heitto [c], Pontus Roldin [d], Taina Yli-Juuti [c], Christophe Duwig [e]

[a] Department of Environmental Science and Bolin Centre for Climate Research, Stockholm University, SE-10691 Stockholm, Sweden
[b] Swedish Meteorological and Hydrological Institute, SE-60176 Norrköping, Sweden
[c] Department of Applied Physics, University of Eastern Finland, 70211 Kuopio, Finland
[d] Division of Nuclear Physics, Department of Physics, Lund University, P. O. Box 118, SE-221 00 Lund, Sweden
[e] Department of Engineering Mechanics, KTH Royal Institute of Technology, SE-10044 Stockholm, Sweden

ABSTRACT

Sulfur and nitrogen oxides (SO_x and NO_x) are harmful pollutants emitted into the atmosphere by industry and transport sectors. In addition to being hazardous gases, SO_x and NO_x form sulfuric and nitric acids which contribute to the formation of airborne particulate matter through nucleation and condensation, hence magnifying the environmental impact of these species. In this work, we build a modeling framework for utilizing this phenomenon for low-temperature exhaust gas cleaning. It has been reported that ammonia gas can be used to facilitate particle formation from the aforementioned acids, and thus remove these gaseous pollutants by converting them into ammonium sulfate and nitrate particles. Here we provide comprehensive modeling tools for applying this idea to exhaust gas cleaning by combining detailed models for nucleation, gas–particle mass exchange and particle population dynamics. We demonstrate how these models can be used to find advantageous operating conditions for a cleaning unit. In particular, the full model is computationally cheap and enables optimization of the particle formation efficiency and particle growth, hence ensuring sufficient conversion of gaseous pollutants into collectable particulate matter. This constitutes a ground for future engineering tools for designing next-generation sustainable exhaust gas cleaners.

1. Introduction

Harmful pollutants released into the atmosphere by various industries, vehicles and ships are a major environmental and health problem. Air pollution is considered to be the single largest environmental health risk worldwide, estimated to cause one in every nine deaths occurring annually.[1] The dominant components of air pollution include sulfur and nitrogen oxides (SO_x and NO_x, respectively), volatile organic compounds (VOCs) and particulate matter (PM). In addition to being directly harmful to human health and to the environment, SO_x and NO_x contribute to the formation of secondary aerosol particles with further adverse health effects. In the atmosphere, SO_x and NO_x are oxidized in the presence of water into sulfuric and nitric acids (H_2SO_4 and HNO_3, respectively), which are condensable vapors that tend to convert into particulate matter.[2] These airborne particles are linked to respiratory and cardiovascular diseases and consequently increased mortality.[2,3] In addition to adverse health effects, aerosol particles have a significant role in regional and global climate dynamics, and have been identified as a critical component of global warming assessments.[4,5] Pollution emissions have a direct and well-known effect on particle formation. For example, a significant increase in aerosol particle number and size can be observed with the release of sulfur-containing ship exhaust,[6] and a clear correlation between particle concentration and the gas-phase sulfuric acid content of exhaust has been reported.[7,8] The gas-to-particle conversion, including particle nucleation and condensational growth, is enhanced by atmospheric base species such as ammonia (NH_3) especially at lower gas-phase acid concentrations. This is an important factor as it enables particle formation also when the pollution is dispersed and well diluted. Bases have a critical enhancing effect on both the initial nanoparticle nucleation[9] and the subsequent particle growth.[10] Co-condensation of ammonia decreases the volatility of the acids by ammonium sulfate and nitrate formation in the particles, thus suppressing the evaporation of the acids back into the gas phase. While the particle formation process has a

negative environmental impact through air pollution, it can be taken advantage of when triggered in a controlled environment for capturing SO_x and NO_x at the source.

Regulations for controlling and mitigating pollutant emissions are becoming more stringent as the understanding of the health and climate effects increases. Abatement strategies[11,12] aim to substantially cut emissions from, for instance, maritime traffic which is a major source of SO_x, NO_x and PM.[13] However, ship emission limits are still very far above similar regulations for automotive, and there is a need for new solutions to limit emissions and accompany future marine regulations. Efficient multi-pollutant emission control for marine engines, gas turbine applications, food industry and thermal power plants requires novel cost-effective flue gas cleaning technologies operating at low gas temperatures (below 600 K). Established post-combustion technologies for NO_x removal such as Selective Catalytic Reduction (SCR) and Selective Non-Catalytic Reduction (SNCR) are unfeasible for the proposed applications due to catalyst poisoning by SO_x below 300 °C,[14] and to a high operating temperature (above 1100 K),[15] respectively. Without compromising low-temperature operation, Non-Thermal Plasma (NTP) has shown that removal efficiencies of 100% for SO_x and above 93% for NO_x are attainable.[16–18] Pollutants are removed by absorption after conversion of NO into higher oxidation states which are increasingly soluble in water.[19] However, the additional costs for disposing of scrubber water and the environmental impacts of scrubber water discharge[20] could be avoided if the formed H_2SO_4 and HNO_3 could be converted into particulate matter instead of scrubbing. Moreover, methods suitable for low-temperature flue gas are desirable also considering energy efficiency and waste-heat recovery. The performance of waste-heat-recovery systems is expected to increase, thus enabling lower operating temperatures, which is a challenge for the traditional cleaning approaches.

The aforementioned tendency of sulfuric and nitric acids to form airborne particles through interaction with NH_3 can be utilized to improve dry desulfurization techniques, and to capture simultaneously both SO_x and NO_x at the source. Experimental work has shown that the addition of ammonia and water vapors to oxidized exhaust gas can be used to induce the formation of ammonium salt particles.[21,22] The particles can further be collected by traditional separation techniques, such as an electrostatic precipitator, centrifugation or a bag filter,[23] and may furthermore be sold as a bulk chemical (e.g. agricultural fertilizers). Controlling the gas-to-particle conversion, however, requires detailed physical understanding of the process in order to find the best operating conditions and to design the reactor accordingly. Ideally, particle formation should deplete completely the gas-phase acids, as well as the added ammonia, and lead to large enough particles for easy collection. Collecting the pollutants in terms of both particle mass and particle number is preferable, since their health, environment and climate effects depend on both quantities.[2] Moreover, ammonia slip should be avoided because of the negative environmental effects of NH_3 such as eutrophication, but also as NH_3 enhances atmospheric aerosol particle formation, thus affecting aerosol–climate interactions and climate dynamics. The latter effect may be particularly important over remote oceans where there are no strong natural ammonia sources, and potential ammonia emissions can thus be a significant issue.

Characterizing, predicting, controlling and optimizing gas-to-particle conversion involves modeling of complex interlinked processes, including (1) initial nucleation through the formation of molecular clusters from gas-phase molecules, (2) condensational growth of particles, affected by dissolution and chemical reactions in the particle phase, and (3) particle population dynamics, including coagulational growth and scavenging of small clusters and nanoparticles by larger particles. Together these non-linear processes determine the partitioning of condensable compounds in the gas and particle phases, and the number and size distribution of the formed particles. While the gas-phase reactions transforming sulfur and nitrogen oxides into acids have been characterized in previous studies,[18] the challenges in

quantitative predictions of the gas–particle mass transfer processes, especially nucleation, have hampered the development of models simulating the conversion of the acids into aerosol.

This work introduces a new framework, imported from atmospheric chemistry studies, for simulating and exploring the possibilities of dry, low-temperature pollutant capture in exhaust gas by formation of ammonium sulfate and nitrate particles. We apply modeling methods previously developed and used for describing atmospheric aerosols, combining detailed models for nucleation, acid–base condensation chemistry and aerosol population dynamics. Such combination allows accounting for the complete chain of the particle formation phenomena. The models have been extensively validated by atmospheric aerosol studies, and here we adapt them for exhaust gas conditions, demonstrating relevance to operating conditions of an exhaust cleaning unit. In addition, we identify and investigate the key process parameters for understanding the gas cleaning performance.

2. Methods

We build a numerical model framework for predicting the gas–particle interaction and the evolution of the particle size distribution in exhaust gas cleaning applications. To this end, we consider the different processes affecting the particle population as depicted in Fig. 1, describing each process explicitly with no empirical parameterizations. Initial nanoparticle formation is simulated with a molecular clustering model, which is directly coupled to an aerosol dynamics model. This in turn simulates the evolution of a particle population in the presence of nucleation, condensation and dissolutional growth by acids and bases, and coagulation. Gas–particle mass transfer through condensation and evaporation are modeled with thermodynamic solution models. The modeled vapors include sulfuric and nitric acids, ammonia and water, and the model framework covers particle sizes explicitly from sub-1 nm molecular clusters to particles of up to 10 μm. We consider a 0-dimensional box, corresponding to a perfectly stirred reactor. The 0D assumption does not limit the impact as such process models can be used later as a sub-grid-scale closure in a computational fluid dynamics (CFD) framework, and thereby simulate spatial variations in the gas and particle concentrations in a realistic industrial reactor.

The main principles of the nucleation, condensation and aerosol population dynamics models are summarized in Sections 2.1–2.3. For more detailed information on the models and aerosol formation processes, the reader is directed to refs. [24–27] and other references given within these sections. In general, particle formation is a complex and non-linear process which involves simultaneously occurring nucleation, condensation and coagulation sub-processes. These sub-processes can be competitive (for example, both nucleation and condensation consume vapors), parallel (e.g. condensational and coagulational growth of formed particles occur simultaneously but are not competitive), or under some conditions consecutive (for example, if the vapors are rapidly consumed, most particle coagulation may occur after the gas-to-particle conversion). Due to this complexity, sophisticated model set-ups are needed to capture the full dynamics of the aerosol formation process.

2.1. Initial nuclei formation

The initial nucleation through molecular cluster formation from gas-phase molecules is simulated with Atmospheric Cluster Dynamics Code (ACDC), the details and validation of which can be found in refs. [26,28]. As the initial nuclei formation requires strongly clustering species, it is assumed to occur by clustering of H_2SO_4 and NH_3 molecules. HNO_3 is a weaker acid and not expected to contribute at high H_2SO_4 concentrations, and it is thus not included in the ACDC modeling. [29] Briefly, ACDC solves the time evolution of the concentrations of molecular clusters of different compositions considering all dynamic processes among the cluster population. This set of equations is written as
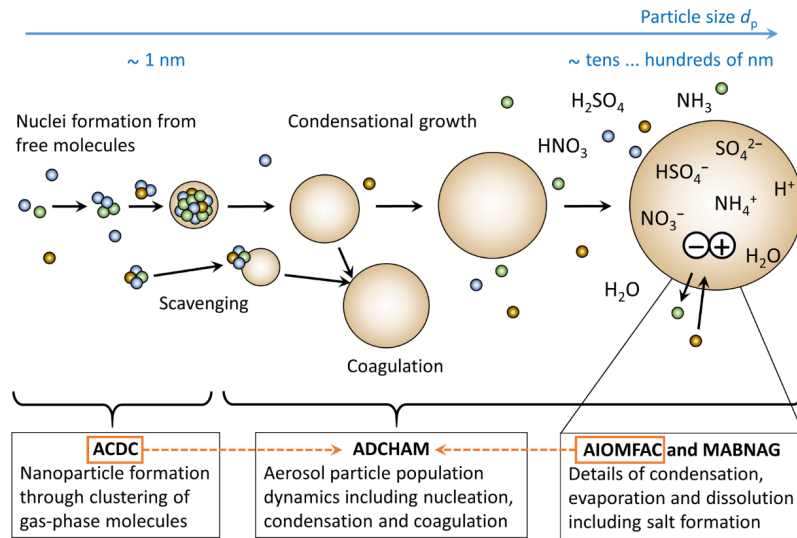
Fig. 1. Schematic presentation of the model framework. The dashed arrows depict the implementation of ACDC and AIOMFAC in ADCHAM. MABNAG is a standalone condensation model which is here used to support the ADCHAM simulations.

$$\frac{\mathrm{d}C_i}{\mathrm{d}t} = \frac{1}{2}\sum_{j<i}\left(\beta_{j,i-j}C_jC_{i-j} - \gamma_{i\to j,i-j}C_i\right) - \sum_j\left(\beta_{i,j}C_iC_j - \gamma_{i+j\to i,j}C_{i+j}\right) - S_iC_i \quad (1)$$

where $\mathrm{d}C_i / \mathrm{d}t$ is the rate of change of the concentration C_i of cluster composition i. The right-hand-side terms correspond to all collision and evaporation processes among the molecules and clusters in which cluster i is either formed or lost. $\beta_{i,i}$ is the rate constant for a collision between clusters or molecules i and j, and $\gamma_{i\to j,i-j}$ is the rate constant for evaporation into products j and $i-j$. S_i is the removal rate constant corresponding to external sinks such as the surfaces of larger particles. The collision constants are here calculated as hard-sphere collision rates, and the evaporation constants are obtained from the formation free energies of the clusters by the detailed balance approach as[30]

$$\gamma_{i+j\to i,j} = \beta_{i,j}\frac{P_{\mathrm{ref}}}{k_{\mathrm{B}}T}\exp\left(\frac{\Delta G_{i+j} - \Delta G_i - \Delta G_j}{k_{\mathrm{B}}T}\right) \quad (2)$$

where ΔG_i is the Gibbs free energy of formation of cluster i, calculated at reference pressure P_{ref}, T is the temperature and k_{B} is the Boltzmann constant. The energies ΔG_i are obtained from available computational chemistry data sets calculated with quantum chemical methods. In the absence of comprehensive experimental techniques, such calculations are the only approach for obtaining thermochemical data for small clusters. The modeled cluster set includes H_2SO_4–NH_3 clusters containing up to 5 H_2SO_4 and 5 NH_3 molecules. Relative humidity is taken into account by including clusters containing water molecules and calculating the effective rate constants over cluster hydrate distributions, as described by ref. [31]. The particle formation rate is obtained as the rate of stable clusters growing out of the ACDC simulation size range, that contain at least 6 H_2SO_4 and 5 NH_3 molecules,[26] corresponding to a nanoparticle diameter of ca. 1.1 nm.

As cluster evaporation rates (Eq. (2)) have a major effect on the cluster concentrations and consequently on the formation rate, we used the currently most accurate quantum chemical data set, computed at the DLPNO-CCSD(T)/aug-cc-pVTZ//ωB97X-D/6-31++G(d,p) level of theory,[32] to calculate the rates. In addition, sensitivity tests were performed by applying a previous data set, computed with an alternative

quantum chemical method, namely RICC2/aug-cc-pV(T + d)Z//B3LYP/CBSB7.[30] The DLPNO method is physically more solid but has a tendency towards over-prediction of evaporation rates; the RICC2 method tends to under-predict evaporation.[33]

2.2. Gas–particle mass transfer

The gas–particle interactions for nanoparticles larger than the clusters covered by ACDC are modeled with the aerosol dynamics, gas- and particle-phase chemistry kinetic multilayer model ADCHAM,[25,34] and the Model for Acid–Base chemistry in NAnoparticle Growth (MABNAG).[27] ADCHAM simulates the evolution of the size-binned particle distribution considering the simultaneous effects of nucleation, condensation and coagulation, and is used as the primary modeling tool together with ACDC. MABNAG is a standalone model that simulates the condensational growth of a particle of given size and composition, and is used as an additional model to compare against ADCHAM. ADCHAM and MABNAG differ slightly in the applied assumptions and thermochemical details (see below), and thus we chose to test both models in order to verify the ADCHAM results. MABNAG was also applied to test the sensitivity of condensational growth to simulation parameters in the absence of effects originating from other aerosol dynamics processes (Section 2.3). The treatment of condensation in ADCHAM and MABNAG are summarized below, and the modeling of simultaneous nucleation, condensation and coagulation by ADCHAM is discussed in Section 2.3.

Net condensation (or evaporation) is generally determined from the gas phase concentrations and the saturation vapor pressures P_{sat} (or equivalently the saturation vapor concentrations $C_{\mathrm{sat}} = P_{\mathrm{sat}} / (k_{\mathrm{B}}T)$) of the compounds over the given particle-phase composition. The saturation vapor pressures are based on thermodynamic solution models which calculate the activity coefficients of the dissolved inorganic ions (here HSO_4^-, SO_4^{2-}, NO_3^-, NH_4^+ and H^+) and water in the particle phase. In the present simulations, the particle phase is assumed to be liquid, i.e. an aqueous solution of the ions is considered. As H_2SO_4 is a strong acid, it is assumed to always dissociate at least once, i.e. only HSO_4^- and SO_4^{2-} and

no H_2SO_4 can exist in the solution.

ADCHAM employs the Aerosol Inorganic-Organic Mixtures Functional groups Activity Coefficients model[35] (AIOMFAC) to determine the saturation vapor concentrations of HNO_3 and NH_3 over each particle size. H_2SO_4 is a very strong acid, which at RH $\geq$ 10% and in the presence of ammonia is commonly assumed to be effectively non-volatile,[36] and its condensation is thus treated as an irreversible process in ADCHAM. The partitioning of ammonia in the gas and particle phases is solved assuming that the particulate ammonia is in thermodynamic equilibrium with the gas-phase ammonia for each particle size.

In MABNAG, the saturation vapor pressures are obtained from the Extended Aerosol Inorganics Model (E-AIM; ref. [37] and references therein). Similarly to AIOMFAC, E-AIM calculates acid dissociation and base protonation in the condensed phase based on equilibrium for these reactions, however applying somewhat different approaches to obtain the parameters involved. MABNAG assumes equilibrium partitioning for ammonia and water similarly to ADCHAM, but calculates the saturation vapor pressure also for H_2SO_4 instead of assuming completely irreversible condensation.

The final saturation vapor concentration $C_{p,n}^{eq}$ of species n over the surface of a nanoparticle of a given size is obtained by adding the size-dependent Kelvin factor, which accounts for increased evaporation from smaller particles due to their larger surface-to-volume ratio.[24] For the dynamically condensing species, namely H_2SO_4 and HNO_3, the change in particle mass m_p due to condensation of species n is solved from the mass fluxes

$$\frac{dm_{p,n}}{dt} = 2\pi (d_p + d_n)(D_p + D_n)f_{p,n}m_n(C_n - C_{p,n}^{eq}) \qquad (3)$$

where d_p and d_n are the diameters of the particle and the vapor species, D_p and D_n are their diffusivities, $f_{p,n}$ is the transition regime correction factor, m_n is the molecular mass of the vapor and C_n is the ambient vapor concentration (for more details, see e.g. ref. [38]). In ADCHAM, the evolution of particle size and composition is solved using the analytic predictor of condensation (APC) scheme and predictor of non-equilibrium growth (PNG),[25,39] while MABNAG applies the Matlab ode23 solver.

2.3. Particle population dynamics

As the high vapor concentrations are expected to result in high numbers of formed nanoparticles, the growth of the particle population is likely to be affected by coagulation in addition to the uptake of vapors, thus making size distribution modeling necessary. ADCHAM simulates the time evolution of the distribution by numerically solving the aerosol general dynamic equation

$$\frac{\partial c(v,t)}{\partial t} = -\frac{\partial}{\partial v}\left(\frac{dv}{dt} \cdot c(v,t)\right) + \frac{1}{2}\int_{v_0}^{v-v_0} \beta(v-v',v')c(v-v',t)c(v',t)dv'$$
$$- c(v,t)\int_{v_0}^{\infty} \beta(v',v)c(v',t)dv' - S(v)c(v,t) + J_0(v)\delta(v-v_0) \qquad (4)$$

where $c(v,t)$ is the number concentration density of particles of volume v. The five terms correspond to condensational growth, formation and loss of size v via particle coagulation, where $\beta(v,v')$ is the coagulation rate constant between sizes v and v', possible sink of particles analogously to Eq. (1), and production of new particles of size v_0 at formation rate J_0, respectively. To obtain a detailed representation of the size distribution, the distribution is discretized into 200 logarithmically spaced size bins from 1.1 nm to 10 μm.

As the initial particle formation and the subsequent growth occur at different time scales, an adaptive time step was applied in ADCHAM. By default, a time step of 10^{-9} s is used based on its good performance against tests conducted with shorter time steps, but the step is allowed to increase as the evolution of the particle distribution becomes slower after the initial nucleation. The length of the step is determined by integrating each time interval twice: in a single step Δt and in two steps $\Delta t / 2$. The actual simulation step is adapted based on the maximum relative difference ε_{max} between the results and a set tolerance of $\varepsilon_{def} = 10^{-3}$ as $\Delta t_{sim} = \max (10^{-9} \text{ s}, 0.8 \times (\varepsilon_{def} / \varepsilon_{max})^{1/2} \times \Delta t)$.[40]

The formation rate of new nuclei is obtained through a coupling to an ACDC module that keeps track of the time-dependent molecular cluster concentrations. At each time step, the concentrations of H_2SO_4 and NH_3 vapors, and the scavenging sink caused by the larger particles modeled by ADCHAM are given as input to the ACDC module. The module simulates the evolution of the cluster concentrations for the given time at these conditions by solving the set of equations given by Eq. (1), and gives as output the number of stable nanoparticles that grow out of the range simulated by ACDC. These new particles are inserted to the lowest size bin of ADCHAM. The scavenging sink accounts for the losses of clusters onto the larger particles, and its dependence on cluster size is approximated as $(d_p / d_{ref})^{-1.6} \times S_{ref}$, where d_p is the cluster mass diameter, and d_{ref} and S_{ref} are a reference diameter and loss rate, here taken to be those of a H_2SO_4 molecule.[41] In this way, S_{ref} is readily available from ADCHAM as the condensation frequency of H_2SO_4 onto the particle size distribution.

2.4. Simulation conditions

We consider a low-temperature exhaust gas environment, with the operating conditions listed in Table 1. The initial conditions assume that SO_x and NO_x have been completely oxidized to H_2SO_4 and HNO_3. Gas-phase reactions involving e.g. SO_2 and SO_3 are complex, and are outside the scope of the present work. The temperature (T) and relative humidity (RH) values are chosen to comply with the thermodynamic data available for H_2SO_4–HNO_3–NH_3 solutions. Namely, we focus on temperatures below 370 K and RHs of 10% or higher (Table 1). Such conditions are realistic for an energy-efficient ship exhaust stream with waste-heat recovery and very challenging for established gas cleaning techniques.

3. Results and discussion

Results obtained with the default ADCHAM–ACDC set-up at the conditions given in Table 1 are presented in Sections 3.1–3.3. Sensitivity tests performed with different molecular cluster data for the ACDC module within the ADCHAM–ACDC combination, and with the stand-alone MABNAG condensation model are discussed in Section 3.4. The effects of the parameters listed in Table 1 on the pollutant conversion process are discussed in Sections 3.1–3.3 and summarized in Table 2. In the text, the number concentrations of gases (ppm) and particles (cm^{-3}) are generally referred to as C, and the concentration of a specific gas-phase species X is referred to as [X].

Table 1

Test conditions used for the present study. The base case values are used for other variables in test simulations in which the effect of varying a specific variable is studied.

Variable	Range / Validity range		Base case
	ACDC and ADCHAM	MABNAG	
$[H_2SO_4]_{init}$	10, 100 ppm		10 ppm, 100 ppm
$[HNO_3]_{init}$	10, 100, 1000 ppm		10 ppm, 100 ppm
$[NH_3]_{init}$	30–2800 ppm		$2 \times [H_2SO_4]_{init} + [HNO_3]_{init}$*
T	300–370 K	300–330 K	330 K
RH	10–90%		10%

* Corresponding to stoichiometric conditions, i.e. the theoretical minimum amount required to neutralize the acids to secure a potentially complete conversion of both the acids and the injected ammonia.

Table 2

Summary of the effects of increasing the values of different variables on the residual gaseous HNO_3 and NH_3 pollutants and on the final mean particle size for the present simulation conditions. Upwards and downwards arrows refer to increasing and decreasing effects, respectively.

Increased variable	Effect on		
	Residual HNO_3	Residual NH_3	Mean particle size
$[H_2SO_4]$ and $[HNO_3]$	Depends on conditions	Depends on conditions	↑
$[NH_3]$	↓	↑	No significant effect
T	↑*	↑*	No significant effect
RH	↓	↓	No significant effect
Residence time	↓ (in a time scale of ~ milliseconds)	↓ (in a time scale of ~ milliseconds)	↑ (in a time scale of ~ seconds)

* Expected general trend; the detailed effects may depend on conditions.

3.1. Effects of nucleation, condensation and coagulation on the gas and particle phases

We first investigate the effects of the simultaneous nucleation, condensation and coagulation on the gas concentrations and on the particle size distribution in order to assess the relative importance of these sub-processes as a function of time. Fig. 2 and Fig. 3 depict the time evolution of the particle population and the gas reduction, respectively, at initial acid concentrations of either $[H_2SO_4]_{init} = [HNO_3]_{init} = 10$ ppm or 100 ppm. At the studied conditions, the nucleation period during which the initial particles form is limited to the first sub-second time window (Fig. 2a). The vapor concentrations decrease (Fig. 3) due to nucleation and condensation onto the formed particles, after which coagulation becomes the dominant process, resulting in a decreasing trend in the total particle number (Fig. 2b). As the particles coagulate, the mean particle size and the spread in the size distribution increase. The coagulational growth rate depends on the particle size distribution and becomes low after a couple of seconds, resulting in an approximately constant size distribution (Fig. 2c). While the quantitative concentrations and time scales depend on the initial acid concentrations, the pollutant conversion process is qualitatively similar for the two cases.

3.2. Reduction of gas-phase pollutants

In the simulations, the gas-phase compounds condense on the formed nanoparticles during and after the initial strong nucleation, and rapidly reach equilibrium with the particle phase (Fig. 3). At the conditions of Fig. 3, the equilibrium gas-phase concentrations are approximately a couple of orders of magnitude lower than the initial concentrations, thus corresponding to a ca. 99% conversion of the initial concentrations to particulate matter. However, the residual concentrations corresponding to these relative reductions are notable from the environmental impacts perspective, and further reductions are desirable. In this section, we seek
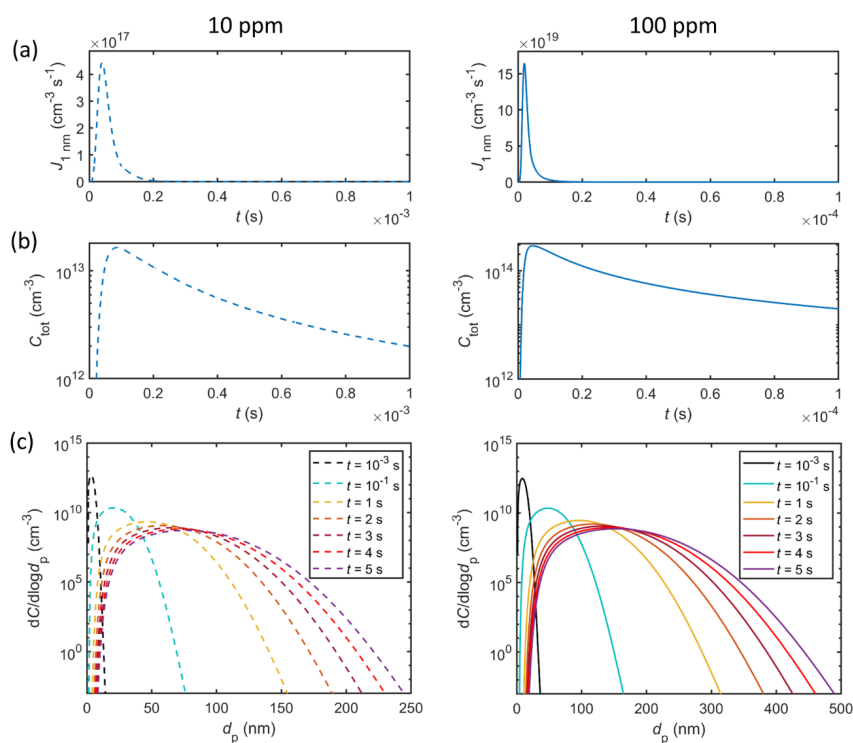
Fig. 2. Panels (a) and (b): Formation rate of nanoparticles of 1 nm (panel (a)) and total particle number (panel (b)) as a function of time at $T = 330$ K, RH = 10% and $[NH_3]_{init} = 2 \times [H_2SO_4]_{init} + [HNO_3]_{init}$. Panel (c): Particle number concentration density as a function of particle size at different times. Panels with dashed and solid lines correspond to $[H_2SO_4]_{init}$ and $[HNO_3]_{init}$ of 10 ppm and 100 ppm each, respectively.
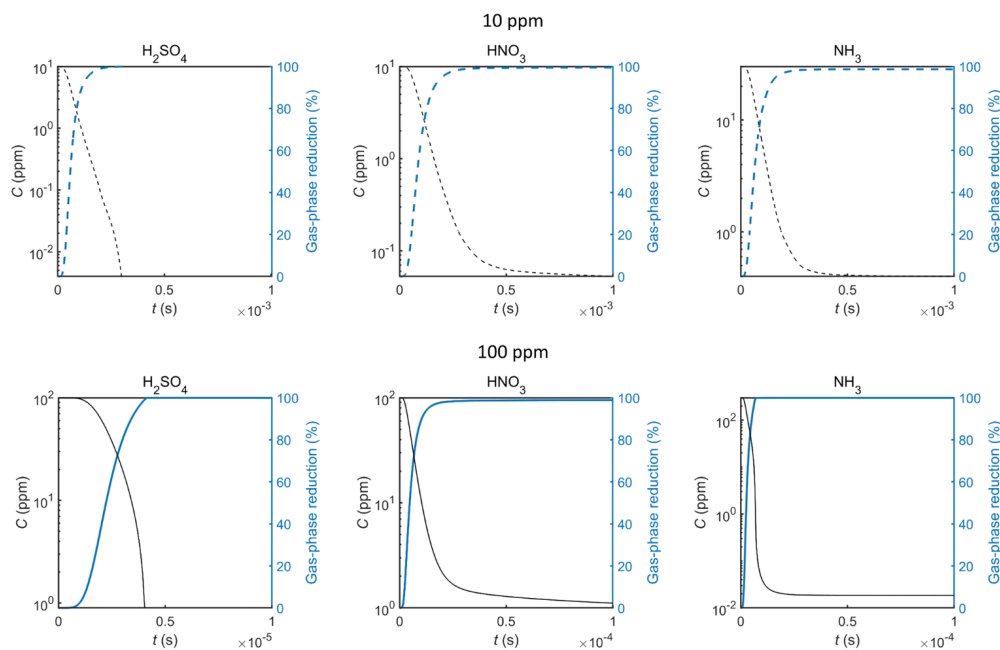
Fig. 3. Gas-phase concentrations of H_2SO_4, HNO_3 and NH_3 (thin black lines; left-hand side axes) and the relative changes in the concentrations with respect to the initial conditions (thick blue lines; right-hand side axes) as a function of time at $T = 330$ K, RH = 10% and $[NH_3]_{init} = 2 \times [H_2SO_4]_{init} + [HNO_3]_{init}$. Panels with dashed and solid lines correspond to $[H_2SO_4]_{init}$ and $[HNO_3]_{init}$ of 10 ppm and 100 ppm each, respectively. (For interpretation of the references to colour in this figure legend, the reader is referred to the web version of this article.)

to identify the parameters enabling the maximum reduction of the gas-phase pollutants. Since H_2SO_4 is very low-volatile and thus assumed to be taken up irreversibly by particles larger than 1 nm within ADCHAM (see discussion in Section 3.4), we focus on HNO_3 and NH_3.

Fig. 4 shows the effects of NH_3 concentration, temperature and RH on the reductions of the gas-phase nitric acid and ammonia. Ammonia has an essential role in binding HNO_3 to the particle phase through salt formation: the consumption of HNO_3 is enhanced at higher NH_3 concentrations, with the absolute final $[HNO_3]$ decreasing by several orders of magnitude when $[NH_3]$ is increased beyond the stoichiometric level $2 \times [H_2SO_4]_{init} + [HNO_3]_{init}$ (Fig. 4a). This means that the theoretical minimum amount of NH_3 needed for complete sulfate and nitrate formation is not sufficient (due to the fact that HNO_3 and NH_3 are volatile), and excess ammonia is required for more efficient HNO_3 removal. However, this comes at the cost of increasing also the residual $[NH_3]$ that remains in the gas phase after the condensation and equilibration (Fig. 4a), and thereby the potential emissions of NH_3.

The effect of temperature in the simulations is somewhat more complex: while gas-to-particle conversion is generally more efficient at lower temperatures, the effect on the reduction of HNO_3 may depend on the absolute pollutant concentrations. Fig. 4b shows a small increase in the residual $[HNO_3]$ for $[HNO_3]_{init} = 100$ ppm when the temperature is decreased from 350 K to 330 K. This can be understood through the increasing effect on nucleation: more nuclei take up more ammonia together with H_2SO_4, resulting in less ammonia available for binding HNO_3 (right-hand side panel of Fig. 4b). In general, temperature can be expected to have a notable effect in terms of both absolute and relative reductions of the gas-phase species at many conditions. However, it must be noted that the available thermodynamic models for

condensation become more uncertain at higher temperatures, and benchmark comparisons against measurements, performed at such conditions, are needed to quantify the temperature effects. Finally, relative humidity has a somewhat smaller effect on the gas-to-particle conversion at these simulation conditions (Fig. 4c), with the residual $[HNO_3]$ and $[NH_3]$ slightly decreasing with increasing RH.

Gas-to-particle conversion is generally more sensitive to changes in the ambient conditions at conditions that are unfavorable to the process, and less sensitive at conditions that are favorable. That is, the process often exhibits a saturation-type behavior. As both nucleation and condensation are reduced at higher temperatures and at lower gas concentrations, the effects of $[NH_3]$ and RH were additionally studied at such more unfavorable conditions, namely at 370 K and $[H_2SO_4]_{init} = [HNO_3]_{init} = 10$ ppm (Fig. 5). This can be expected to give an upper-limit estimate for the sensitivity of the conversion process to these parameters for the present simulation set-up. At these conditions, the final HNO_3 and NH_3 concentrations at the studied initial $[NH_3]$ and RH are generally higher or of the same order as at the conditions of Fig. 4. However, the conversion efficiency of the gases at the base case values of $[NH_3]$ and RH ($2 \times [H2SO4]_{init} + [HNO3]_{init}$ and 10%, respectively) is weaker at 370 K than at lower temperatures: at 370 K, ca. 85–90% of $[HNO3]$ and $[NH_3]$ is converted to particles at $[H_2SO_4]_{init} = [HNO_3]_{init} = 10$ ppm, while at 330 and 350 K the reductions are 95–100% (panel (b) in Fig. 4). At 370 K, the increases in $[NH_3]$ and RH increase the relative reductions notably, with the conversion efficiency of HNO_3 increased from ca. 85% to close to 100% (left-hand side panels of Fig. 5). Adjusting $[NH_3]$ or RH is thus an efficient approach to improve the pollutant conversion at such conditions. In general, when the effects of increased $[NH_3]$ and RH are similar, RH is a better option as it also decreases the
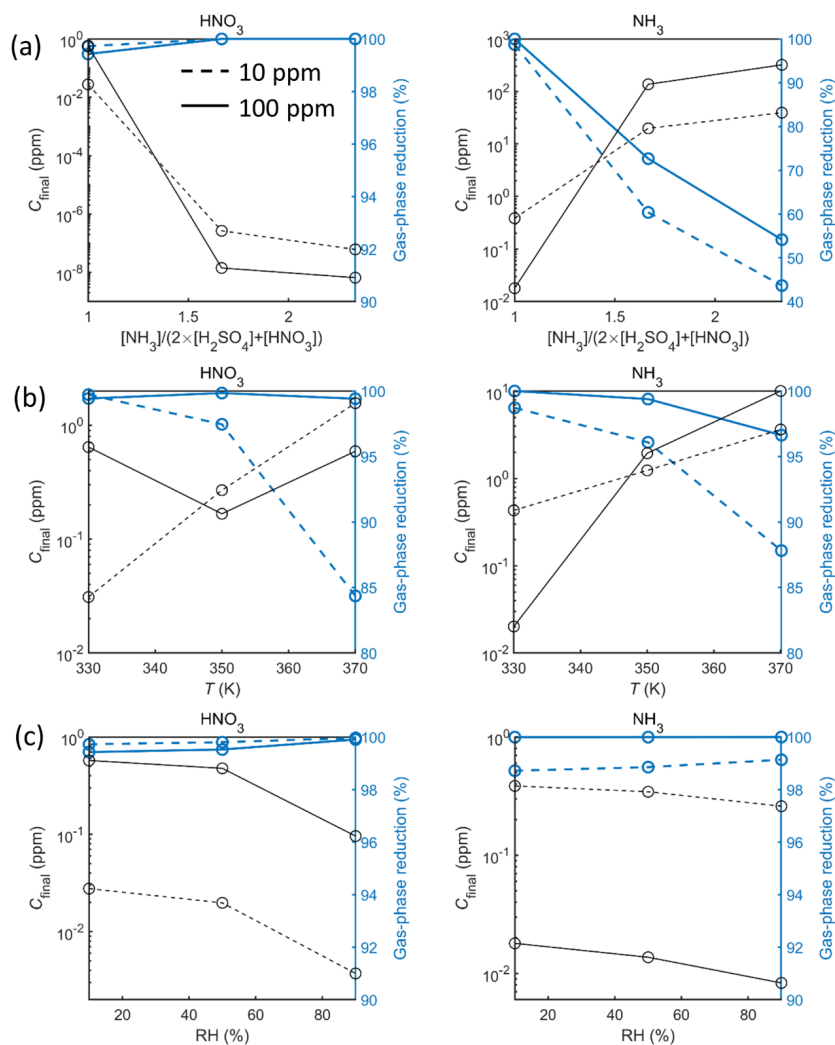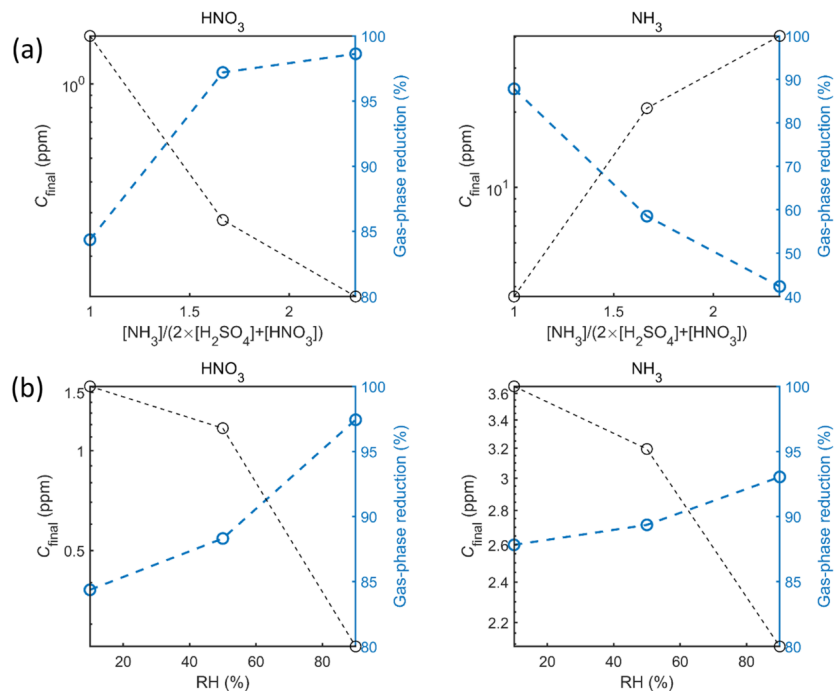
Fig. 4. Effects of added NH_3 concentration (panel (a)), temperature (panel (b)), and RH (panel (c)) on the reduction of nitric acid and ammonia. When one of the parameters is varied, the others are fixed to their base case values (Table 1). Dashed and solid lines correspond to $[H_2SO_4]_{init}$ and $[HNO_3]_{init}$ of 10 ppm and 100 ppm each, respectively.

excess NH_3 instead of increasing it (right-hand side panels of Fig. 5).

Finally, we tested a simulation case at a higher $[HNO_3]_{init}$. For example marine engines can produce high NO_x concentrations,[17] and generally operate at higher temperatures. Therefore, we included a test simulation performed at $T = 370$ K, $[H_2SO_4]_{init} = 100$ ppm, and $[HNO_3]_{init} = 1000$ ppm, as shown in Supplementary Information Section 3. While the results are generally similar to those of the other cases, the sizes of the formed particles are larger due to the increased HNO_3 condensation. In addition, the higher $[NH_3]_{init}$ required to compensate for the higher $[HNO_3]_{init}$ leads to higher residual $[NH_3]$.

The overall results of this section are collected in Table 2 along with

the results on the mean particle size (Fig. 2; Section 3.3). The main conclusions can be summarized as follows: (1) the so-called stoichiometric NH_3 level ($2 \times [H_2SO_4]_{init} + [HNO_3]_{init}$) is not enough for complete pollutant conversion. Increasing $[NH_3]$ beyond this level enhances the conversion but increases the unwanted residual ammonia. (2) Simultaneous enhancement in the acid conversion and decrease in the residual ammonia can be achieved by adjusting T or RH. The quantitative enhancements for these different means depend on the exact conditions, but are comparable at many conditions.

Fig. 5. Effects of added NH_3 concentration (panel (a)) and RH (panel (b)) on the reduction of nitric acid and ammonia at $T = 370$ K and $[H_2SO_4]_{init} = [HNO_3]_{init} = 10$ ppm, with other simulation settings as in Fig. 4.

3.3. Size distribution of formed particles

The final particle size distribution is largely determined by coagulation processes and hence by the residence time. The longer the residence time, the larger the mean particle size and the wider the size distribution. Fig. 6 shows the time evolution of the sizes corresponding to the maximum concentration and to 5% and 95% of the cumulative size distribution in terms of both particle number and particle mass. That is, collecting the shaded size ranges corresponds to removing 90 percent of the particles and their mass. The absolute spread increases quickly
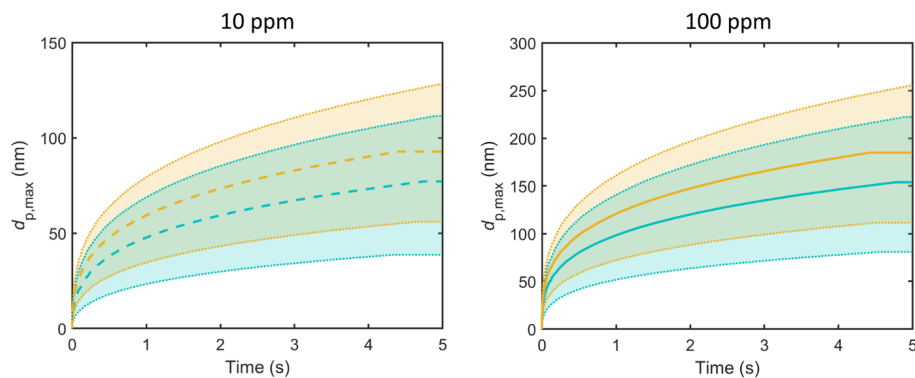
Fig. 6. Particle diameters corresponding to the maximum number (turquoise; lower line and lower shaded area) and mass (orange; upper line and upper shaded area) concentrations as a function of time at $T = 330$ K, RH = 10% and $[NH_3]_{init} = 2 \times [H_2SO_4]_{init} + [HNO_3]_{init}$. The shaded areas cover 90% of the total number and mass, where the dotted lines limiting the areas correspond to the sizes below which 5% and 95% of the total concentrations lie. Panels with dashed and solid lines correspond to $[H_2SO_4]_{init}$ and $[HNO_3]_{init}$ of 10 ppm and 100 ppm each, respectively. (For interpretation of the references to colour in this figure legend, the reader is referred to the web version of this article.)

with time especially at higher [H_2SO_4] and [HNO_3] (right-hand side panel in Fig. 6), which affects the optimal residence time for a given particle collection method. For instance, if an electrostatic precipitator with a specific size-dependent collection efficiency is used, shorter residence times are desirable to prevent the size distribution from spreading to sizes that are not efficiently collected.

The size distribution is not sensitive to changes in [NH_3], *T*, and RH at the studied conditions. The effects of these parameters on, for example, the size ranges covering 90% of the particle number and mass (Fig. 6) are minor compared to the overall spreads.

3.4. Additional simulations and sensitivity tests

Additional simulations conducted at the conditions of Fig. 2 and Fig. 3 applying the RICC2 quantum chemistry data are presented in Figures S1 and S2 in the Supplementary Information. As expected, the tests show differences in the initial particle number and consequently in the gas–particle partitioning due to the tendency of the RICC2 method to predict stronger and faster cluster formation. For RICC2, [HNO_3] first decreases faster than for DLPNO, but remains then at a higher level, presumably due to less NH_3 available after the initial nucleation. However, the test demonstrates that even with quantitative changes in the molecular cluster input data, the general results for the initial particle formation process remain similar. Of the two applied data sets, DLPNO is more reliable and is thus expected to yield quantitatively more accurate results.

Results obtained with the condensational growth model MABNAG are in line with the ADCHAM simulations. Fig. 7 shows a MABNAG simulation corresponding to the conditions of the upper panel of Fig. 3. The reduction of the gas-phase compounds and the time scale of the condensation are similar to Fig. 3. The absolute reductions are somewhat lower than in ADCHEM, which can be due to (1) nucleation not consuming the vapors in MABNAG, and (2) the constant particle number concentration which is slightly lower than the peak values in ADCHAM. MABNAG tests with varying RH and [NH_3]$_{init}$ also give results similar to Fig. 4 (not shown): increasing RH leads to a modest (less than an order of magnitude) decrease in [HNO_3] and [NH_3], while increasing the initial [NH_3] causes a decrease of a couple of orders of magnitude in the final [HNO_3].

Figures S3 and S4 present sensitivity tests related to the condensation processes, performed with MABNAG. The saturation vapor pressures P_{sat} are essential parameters for condensation modeling. While the saturation vapor pressure $P_{sat,HNO3}$ of HNO_3 over inorganic solutions of H_2SO_4, HNO_3, NH_3 and H_2O is generally well-known, the available thermodynamic solution models may become more uncertain at high temperature and low RH, and we therefore tested the effects of varying this parameter. As can be expected, increasing $P_{sat,HNO3}$ and thus the volatility of

HNO_3 leads to higher residual HNO_3 and NH_3 concentrations (Figure S3). However, uncertainties of more than ca. 1–2 orders of magnitude in $P_{sat,HNO3}$ can be expected to be unlikely. On the contrary, increasing the saturation vapor pressure of H_2SO_4 even by up to a factor of 10^4 has no effect on the results (not shown). This indicates that the pressure is close to zero and thus that H_2SO_4 condensation can be assumed irreversible, as modeled by ADCHAM.

Similarly to ADCHAM, MABNAG shows only very modest particle growth in terms of particle diameter at the studied conditions, suggesting that condensation alone cannot be expected to grow the population to collectable sizes. This is due to the strong nuclei formation, resulting in a high number of particles onto which the condensing vapors are distributed. In order for the initial particles to grow by condensation to sizes comparable to those due to coagulation (Fig. 6), their number concentration should be orders of magnitude lower (Figure S4). At the present simulation conditions, the condensational growth rate in terms of particle diameter is primarily determined by the particle number, and exhibits only minor variations with, for instance, *T* and RH at a given particle concentration (not shown). This demonstrates the importance of modeling the evolution of particle number together with the evolution of particle mass.

Overall, the sensitivity tests suggest that in addition to the thermodynamic parameters governing the gas–particle interactions, quantitative predictions of the gas-to-particle conversion depend also on the initial nucleation description through its effects on the particle number and on the gas-phase concentrations. While the different test cases indicate that the qualitative predictions are robust, accurately constraining the model input parameters would ideally require benchmark measurements of both gases and particles at high [H_2SO_4] and [HNO_3] and high temperature set-ups.

4. Conclusions

Conversion of sulfur and nitrogen species to particulate matter by mixing with ammonia vapor is a promising approach to clean low-temperature exhaust gas without aquatic solutions. The presented model framework for simulation of ammonium sulfate and nitrate particle formation provides tools to assess the performance and optimal operating conditions of such next-generation exhaust gas cleaners. The main factors affecting the conversion of the gas-phase condensable species H_2SO_4 and HNO_3 are temperature, added ammonia concentration and relative humidity. While these parameters control the reduction of the gas concentrations, the resulting particle size distribution is largely determined by the residence time, as coagulation drives particle growth after the equilibration of the condensable vapors. This is relevant for particle collection, and thus the residence time should be optimized according to the growth dynamics and the size-dependent collection
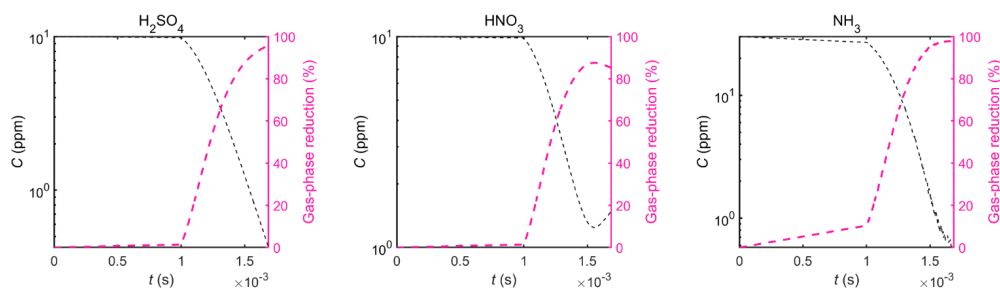

Fig. 7. MABNAG simulations of the gas-phase concentrations of H_2SO_4, HNO_3 and NH_3 (thin black lines; left-hand side axes) and the relative changes in the concentrations with respect to the initial conditions (thick purple lines; right-hand side axes) as a function of time at $T = 330$ K, RH = 10%, [H_2SO_4]$_{init}$ = [HNO_3]$_{init}$ = 10 ppm, [NH_3]$_{init}$ = 2 × [H_2SO_4]$_{init}$ + [HNO_3]$_{init}$, and a total particle concentration of 10^{12} cm^{-3}. (For interpretation of the references to colour in this figure legend, the reader is referred to the web version of this article.)

efficiency. The presented modeling tools can be used to guide benchmark experiments by assessing which types of conditions are most promising to test experimentally, and into which directions the different parameters should be adjusted. Such experiments will be the topic of future work and the next step to assess the performance of the acid conversion. Experimental efforts are also needed to evaluate and further improve the models, particularly at higher temperatures.

This work demonstrates the application of the simulation tools by process-level modeling of nucleation, condensational growth and particle population dynamics. For detailed modeling of particle formation and growth in non-uniform exhaust flows with specific flow geometries, the tools can be embedded in a fluid dynamics model. More complex gas-phase chemistry including oxidation reactions of SO_x and NO_x can be incorporated in the framework when available to include the possible time-dependent production of sulfuric and nitric acids. Finally, while this study focuses on optimizing gas-to-particle conversion for exhaust cleaning purposes, the presented models can also be applied to assess unwanted particulate matter formation in released exhaust downstream the tailpipe for studying the environmental impacts of the emissions.

CRediT authorship contribution statement

Tinja Olenius: Methodology, Software, Investigation, Writing - original draft, Writing - review & edting. **Arto Heitto:** Software, Investigation, Writing - review & edting. **Pontus Roldin:** Methodology, Resources, Writing - review & edting. **Taina Yli-Juuti:** Methodology, Resources, Supervision, Writing - review & edting. **Christophe Duwig:** Conceptualization, Supervision, Writing - review & edting.

Declaration of Competing Interest

The authors declare that they have no known competing financial interests or personal relationships that could have appeared to influence the work reported in this paper.

Data availability

The DLPNO data used in the ACDC simulations is available in the Atmospheric Cluster Database (ACDB) at https://github.com/elmjonas/ACDB. AIOMFAC is available at http://www.aiomfac.caltech.edu/ and https://github.com/andizuend/AIOMFAC. All data and models presented in this study are available from the authors upon request.

Appendix A. Supplementary data

Supplementary data to this article can be found online at https://doi.org/10.1016/j.fuel.2020.120044.

References

[1] World Health Organization. Ambient Air Pollution: A Global Assessment of Exposure and Burden of Disease. Technical Report; WHO: Geneva; 2016.
[2] Fuzzi S, Baltensperger U, Carslaw K, Decesari S, Denier van der Gon H, Facchini MC, et al. Particulate matter, air quality and climate: lessons learned and future needs. Chem Phys 2015;15(14):8217–99. https://doi.org/10.5194/acp-15-8217-2015.
[3] Terzano C, Di Stefano F, Conti V, Graziani E, Petroianni A. Air Pollution Ultrafine Particles: Toxicity beyond the Lung. Eur Rev Med Pharmacol Sci 2010;14(10):809–21.
[4] Myhre G, Shindell D, Bréon FM, Collins W, Fuglestvedt J, Huang J, Koch D, et al., Anthropogenic and Natural Radiative Forcing. In Climate Change 2013: The Physical Science Basis; IPCC, Cambridge, United Kingdom and New York, NY, USA: Cambridge University Press; 2013, p. 659–740.
[5] Boucher O, Randall D, Artaxo P, Bretherton C, Feingold G, Forster P, Kerminen VM, et al., Clouds and Aerosols. In Climate Change 2013: The Physical Science Basis; IPCC, Cambridge, United Kingdom and New York, NY, USA: Cambridge University Press; 2013, p. 571–657.
[6] Viana M, Hammingh P, Colette A, Querol X, Degraeuwe B, Vlieger I, et al. Impact of Maritime Transport Emissions on Coastal Air Quality in Europe. Atmos Environ 2014;90:96–105. https://doi.org/10.1016/j.atmosenv.2014.03.046.
[7] Rönkkö T, Lähde T, Heikkilä J, Pirjola L, Bauschke U, Arnold F, et al. Effects of Gaseous Sulphuric Acid on Diesel Exhaust Nanoparticle Formation and Characteristics. Environ Sci Technol 2013;47(20):11882–9. https://doi.org/10.1021/es402354y.
[8] Srivastava RK, Miller CA, Erickson C, Jambhekar R. Emissions of Sulfur Trioxide from Coal-Fired Power Plants. J Air Waste Manag Assoc 2004;54(6):750–62. https://doi.org/10.1080/10473289.2004.10470943.
[9] Kirkby J, Curtius J, Almeida J, Dunne E, Duplissy J, Ehrhart S, et al. Role of Sulphuric Acid, Ammonia and Galactic Cosmic Rays in Atmospheric Aerosol Nucleation. Nature 2011;476(7361):429–33. https://doi.org/10.1038/nature10343.
[10] Celik S, Drewnick F, Fachinger F, Brooks J, Darbyshire E, Coe H, et al. Influence of Vessel Characteristics and Atmospheric Processes on the Gas and Particle Phase of Ship Emission Plumes. In Situ Measurements in the Mediterranean Sea and around the Arabian Peninsula. Atmospheric Chem Phys 2020;20(8):4713–34. https://doi.org/10.5194/acp-20-4713-2020.
[11] European Commission. Proposal for a Directive of the European Parliament and of the Council on the Reduction of National Emissions of Certain Atmospheric Pollutants and Amending Directive 2003/35/EC. Technical Report; European Commission: Brussels; 2013.
[12] International Energy Agency. Energy and Air Pollution. World Energy Outlook Special Report; OECD / IEA: Paris; 2016.
[13] International Maritime Organization. Revised MARPOL Annex VI : Regulations for the Prevention of Air Pollution from Ships and NOx Technical Code 2008; International Maritime Organization: London; 2009.
[14] Magnusson M, Fridell E, Ingelsten HH. The Influence of Sulfur Dioxide and Water on the Performance of a Marine SCR Catalyst. Appl Catal B Environ 2012;111–112:20–6. https://doi.org/10.1016/j.apcatb.2011.09.010.
[15] Skalska K, Miller JS, Ledakowicz S. Trends in NOx Abatement: A Review. Sci Total Environ 2010;408(19):3976–89. https://doi.org/10.1016/j.scitotenv.2010.06.001.
[16] Mok YS, Lee H-J. Removal of Sulfur Dioxide and Nitrogen Oxides by Using Ozone Injection and Absorption-Reduction Technique. Fuel Process Technol 2006;87(7):591–7. https://doi.org/10.1016/j.fuproc.2005.10.007.
[17] Zhou S, Zhou J, Feng Y, Zhu Y. Marine Emission Pollution Abatement Using Ozone Oxidation by a Wet Scrubbing Method. Ind Eng Chem Res 2016;55(20):5825–31. https://doi.org/10.1021/acs.iecr.6b01038.
[18] Ma S, Zhao Y, Yang J, Zhang S, Zhang J, Zheng C. Research Progress of Pollutants Removal from Coal-Fired Flue Gas Using Non-Thermal Plasma. Renew Sustain Energy Rev 2017;67:791–810. https://doi.org/10.1016/j.rser.2016.09.066.
[19] Wang Z. Energy and Air Pollution. In Comprehensive Energy Systems; Elsevier: Amsterdam, Netherlands, 2018; Vol. 1–5, p. 909–49.
[20] Endres S, Maes F, Hopkins F, Houghton K, Mårtensson EM, Oeffner J, et al. A New Perspective at the Ship-Air-Sea-Interface: The Environmental Impacts of Exhaust Gas Scrubber Discharge. Front Mar Sci 2018;5. https://doi.org/10.3389/fmars.2018.00139.
[21] Tseng C-H, Keener TC, Lee J-Y, Khang S-J. Enhanced Effect of In-Situ Generated Ammonium Salts Aerosols on the Removal of NOx from Simulated Flue Gas. Environ Sci Technol 2001;35(15):3219–24. https://doi.org/10.1021/es001797x.
[22] Basfar AA, Fageeha OI, Kunnummal N, Al-Ghamdi S, Chmielewski AG, Licki J, et al. Electron Beam Flue Gas Treatment (EBFGT) Technology for Simultaneous Removal of SO2 and NOx from Combustion of Liquid Fuels. Fuel 2008;87(8):1446–52. https://doi.org/10.1016/j.fuel.2007.09.005.
[23] Yi H, Hao J, Duan L, Tang X, Ning P, Li X. Fine Particle and Trace Element Emissions from an Anthracite Coal-Fired Power Plant Equipped with a Bag-House in China. Fuel 2008;87(10):2050–7. https://doi.org/10.1016/j.fuel.2007.10.009.
[24] Olenius T, Yli-Juuti T, Elm J, Kontkanen J, Riipinen I. New Particle Formation and Growth: Creating a New Atmospheric Phase Interface. In Physical Chemistry of Gas–Liquid Interfaces; Developments in Physical & Theoretical Chemistry; Elsevier; 2018, p. 315–52.
[25] Roldin P, Swietlicki E, Schurgers G, Arneth A, Lehtinen KEJ, Boy M, et al. Development and Evaluation of the Aerosol Dynamics and Gas Phase Chemistry Model ADCHEM. Atmospheric Chem Phys 2011;11(12):5867–96. https://doi.org/10.5194/acp-11-5867-2011.
[26] Olenius T, Kupiainen-Määttä O, Ortega IK, Kurtén T, Vehkamäki H. Free Energy Barrier in the Growth of Sulfuric Acid-Ammonia and Sulfuric Acid-Dimethylamine Clusters. J Chem Phys 2013;139(8):084312. https://doi.org/10.1063/1.4819024.
[27] Yli-Juuti T, Barsanti K, Hildebrandt Ruiz L, Kieloaho A-J, Makkonen U, Petäjä T, et al. Model for Acid-Base Chemistry in Nanoparticle Growth (MABNAG).

Atmospheric Chem Phys 2013;13(24):12507–24. https://doi.org/10.5194/acp-13-12507-2013.

[28] Almeida J, Schobesberger S, Kürten A, Ortega IK, Kupiainen-Määttä O, Praplan AP, et al. Molecular Understanding of Sulphuric Acid-Amine Particle Nucleation in the Atmosphere. Nature 2013;502(7471):359–63. https://doi.org/10.1038/nature12663.

[29] Liu L, Li H, Zhang H, Zhong J, Bai Y, Ge M, et al. The Role of Nitric Acid in Atmospheric New Particle Formation. Phys Chem Chem Phys 2018;20(25):17406–14. https://doi.org/10.1039/C8CP02719F.

[30] Ortega IK, Kupiainen O, Kurtén T, Olenius T, Wilkman O, McGrath MJ, et al. From Quantum Chemical Formation Free Energies to Evaporation Rates. Atmospheric Chem Phys 2012;12(1):225–35. https://doi.org/10.5194/acp-12-225-2012.

[31] Henschel H, Kurtén T, Vehkamäki H. Computational Study on the Effect of Hydration on New Particle Formation in the Sulfuric Acid/Ammonia and Sulfuric Acid/Dimethylamine Systems. J Phys Chem 2016;120(11):1886–96. https://doi.org/10.1021/acs.jpca.5b11366.

[32] Elm J. An Atmospheric Cluster Database Consisting of Sulfuric Acid, Bases, Organics, and Water. ACS Omega 2019;4(6):10965–74. https://doi.org/10.1021/acsomega.9b00860.

[33] Carlsson PTM, Celik S, Becker D, Olenius T, Elm J, Zeuch T. Neutral Sulfuric Acid-Water Clustering Rates: Bridging the Gap between Molecular Simulation and Experiment. J Phys Chem Lett 2020;11:4239–44. https://doi.org/10.1021/acs.jpclett.0c01045.

[34] Roldin P, Eriksson AC, Nordin EZ, Hermansson E, Mogensen D, Rusanen A, et al. Modelling Non-Equilibrium Secondary Organic Aerosol Formation and Evaporation with the Aerosol Dynamics, Gas- and Particle-Phase Chemistry Kinetic

Multilayer Model ADCHAM. Atmospheric Chem Phys 2014;14(15):7953–93. https://doi.org/10.5194/acp-14-7953-2014.

[35] Zuend A, Marcolli C, Booth AM, Lienhard DM, Soonsin V, Krieger UK, et al. New and Extended Parameterization of the Thermodynamic Model AIOMFAC: Calculation of Activity Coefficients for Organic-Inorganic Mixtures Containing Carboxyl, Hydroxyl, Carbonyl, Ether, Ester, Alkenyl, Alkyl, and Aromatic Functional Groups. Atmospheric Chem Phys 2011;11(17):9155–206. https://doi.org/10.5194/acp-11-9155-2011.

[36] Tsagkogeorgas G, Roldin P, Duplissy J, Rondo L, Tröstl J, Slowik JG, et al. Evaporation of Sulfate Aerosols at Low Relative Humidity. Atmospheric Chem Phys 2017;17(14):8923–38. https://doi.org/10.5194/acp-17-8923-2017.

[37] Wexler AS, Clegg SL. Atmospheric Aerosol Models for Systems Including the Ions H +, NH4+, Na+, SO42−, NO3−, Cl−, Br−, and H2O. J. Geophys. Res. Atmospheres 2002;107(D14):ACH 14-1-ACH 14-14. https://doi.org/10.1029/2001JD000451.

[38] Lehtinen KEJ, Kulmala M. A Model for Particle Formation and Growth in the Atmosphere with Molecular Resolution in Size. Atmospheric Chem Phys 2003;3(1):251–7. https://doi.org/10.5194/acp-3-251-2003.

[39] Jacobson MZ. A Solution to the Problem of Nonequilibrium Acid/Base Gas-Particle Transfer at Long Time Step. Aerosol Sci Technol 2005;39(2):92–103. https://doi.org/10.1080/027868290904546.

[40] Gear CW. Numerical Initial Value Problems in Ordinary Differential Equations; USA: Prentice Hall PTR; 1971.

[41] Lehtinen KEJ, Dal Maso M, Kulmala M, Kerminen V-M. Estimating Nucleation Rates from Apparent Particle Formation Rates and Vice Versa: Revised Formulation of the Kerminen-Kulmala Equation. J Aerosol Sci 2007;38(9):988–94. https://doi.org/10.1016/j.jaerosci.2007.06.009.